Supporting Information for "Tidal Effects on the Longitudinal Structures of the Martian Thermosphere and Topside Ionosphere Observed by MAVEN"

Xiaohua Fang [1], Jeffrey M. Forbes [2], Quan Gan [1], Guiping Liu [3], Scott Thaller [1], Stephen Bougher [4], Laila Andersson [1], Mehdi Benna [5], Francis Eparvier [1], Yingjuan Ma [6], David Pawlowski [7], Scott England [8], and Bruce Jakosky [1]

[1]Laboratory for Atmospheric and Space Physics, University of Colorado, Boulder, Colorado, USA

[2]Ann and H.J. Smead Department of Aerospace Engineering Sciences, University of Colorado, Boulder, Colorado, USA

[3]Space Sciences Laboratory, University of California, Berkeley, California, USA

[4]Department of Climate and Space Sciences and Engineering, University of Michigan, Ann Arbor, Michigan, USA

[5]NASA Goddard Space Flight Center, Greenbelt, Maryland, USA

[6]Department of Earth, Planetary and Space Sciences, University of California, Los Angeles, California, USA

[7]Physics and Astronomy Department, Eastern Michigan University, Ypsilanti, Michigan, USA

[8]Department of Aerospace and Ocean Engineering, Virginia Polytechnic Institute and State University, Blacksburg, VA, USA

Contents of this file

1. Figures S1 to S6

Introduction

Figure S1 shows the spatial distribution of available MAVEN data points for the current study.

Figure S2 provides the context of solar radiation at Mars' orbit, in which the four cases of Ls1-Ls4 have been highlighted. Both the seasonal Sun-Mars distance change and solar activity come into play in controlling the heating and ionizing solar fluxes reaching the Martian atmosphere.

Figure S3 provides the context of atmospheric dust loading, in which Ls1-Ls4 have been marked. It is shown that Ls1-Ls2 are basically dust-free, and Ls3-Ls4 are associated with regional dust storm events.

Figure S4 demonstrates that non-identical SZA and EUV conditions of individual data points within each case actually make little impact on the tidal wave signatures. Therefore, we choose to use the original data (rather than the data scaled after SZA and EUV) in this work for simplicity.

Figure S5 shows that the MAVEN sampling analyzed in this work effectively avoids Martian strong crustal magnetic field regions. Therefore, the potential influence of the crustal field is negligible in our tidal analysis.

Figure S6 shows the altitude profiles of zonal means and tidal wave amplitudes, providing complementary information to Figure 8 of the main text.

References

Fang, X., Ma, Y., Brain, D., Dong, Y., & Lillis, R. (2015). Control of mars global atmospheric loss by the continuous rotation of the crustal magnetic field: A time-dependent MHD study. *Journal of Geophysical Research: Space Physics*, *120*(12), 10–926. doi: 10.1002/2015JA021605

Fang, X., Ma, Y., Masunaga, K., Dong, Y., Brain, D., Halekas, J., ... others (2017). The mars crustal magnetic field control of plasma boundary locations and atmospheric loss: MHD prediction and comparison with MAVEN. *Journal of Geophysical Research: Space Physics*, *122*(4), 4117–4137. doi: 10.1002/2016JA023509

Ma, Y., Fang, X., Russell, C. T., Nagy, A. F., Toth, G., Luhmann, J. G., ... Dong, C. (2014). Effects of crustal field rotation on the solar wind plasma interaction with mars. *Geophysical Research Letters*, *41*(19), 6563–6569.

Montabone, L., Spiga, A., Kass, D. M., Kleinböhl, A., Forget, F., & Millour, E. (2020). Martian year 34 column dust climatology from mars climate sounder observations: Reconstructed maps and model simulations. *Journal of Geophysical Research: Planets*. doi: 10.1029/2019JE006111

Morschhauser, A., Lesur, V., & Grott, M. (2014). A spherical harmonic model of the lithospheric magnetic field of mars. *Journal of Geophysical Research: Planets*, *119*(6), 1162–1188. doi: 10.1002/2013JE004555

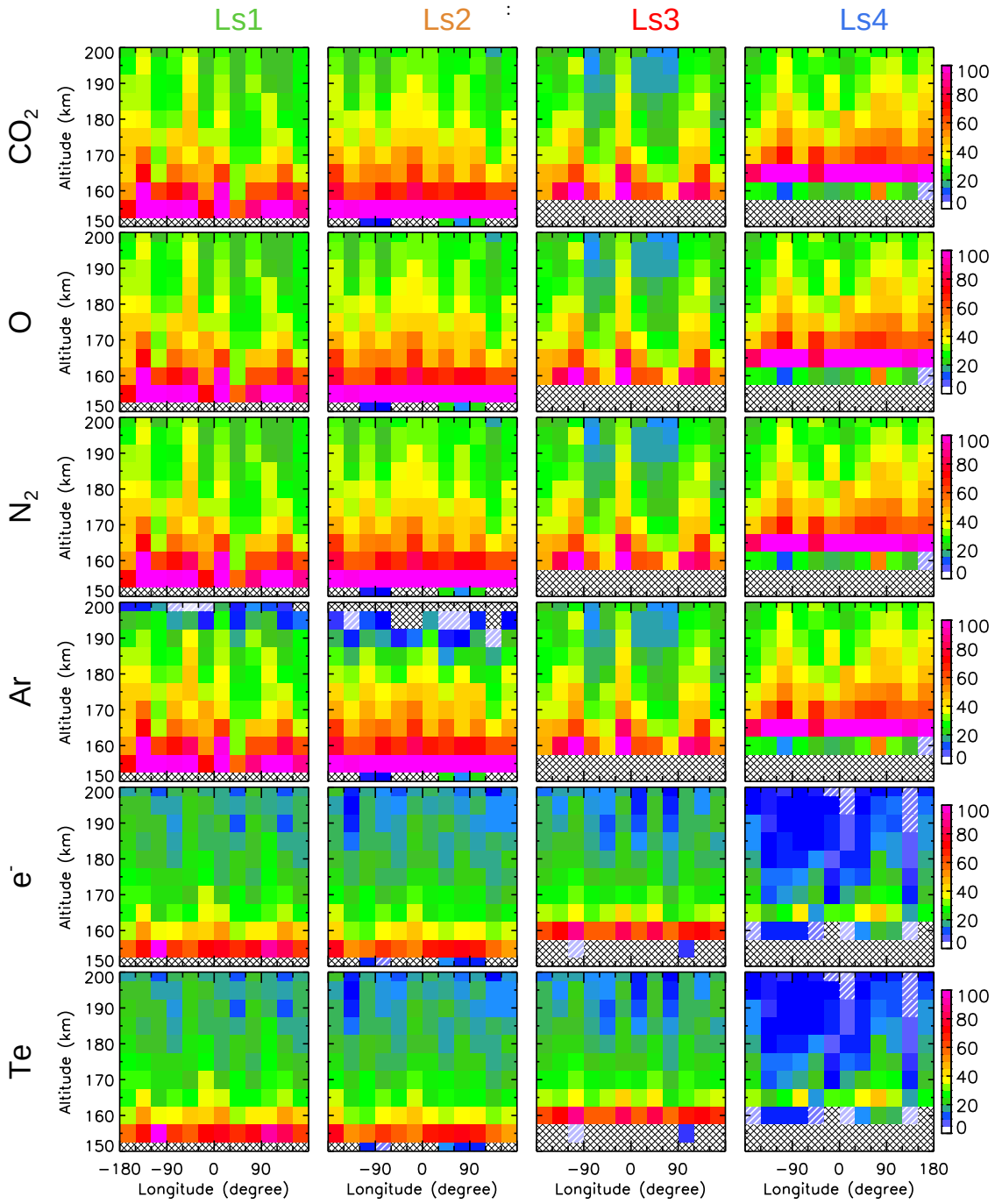

Figure S1. Number of available MAVEN data points as a function of longitude and altitude. The results are given (from left to right) in the four cases of Ls1-Ls4 and (from top to bottom) for CO_2 density, O density, N_2 density, Ar density, electron density, and electron temperature, respectively. The cross-hatched areas indicate missing data. The white-hatched areas indicate the bins where the number of available data points is less than 5.

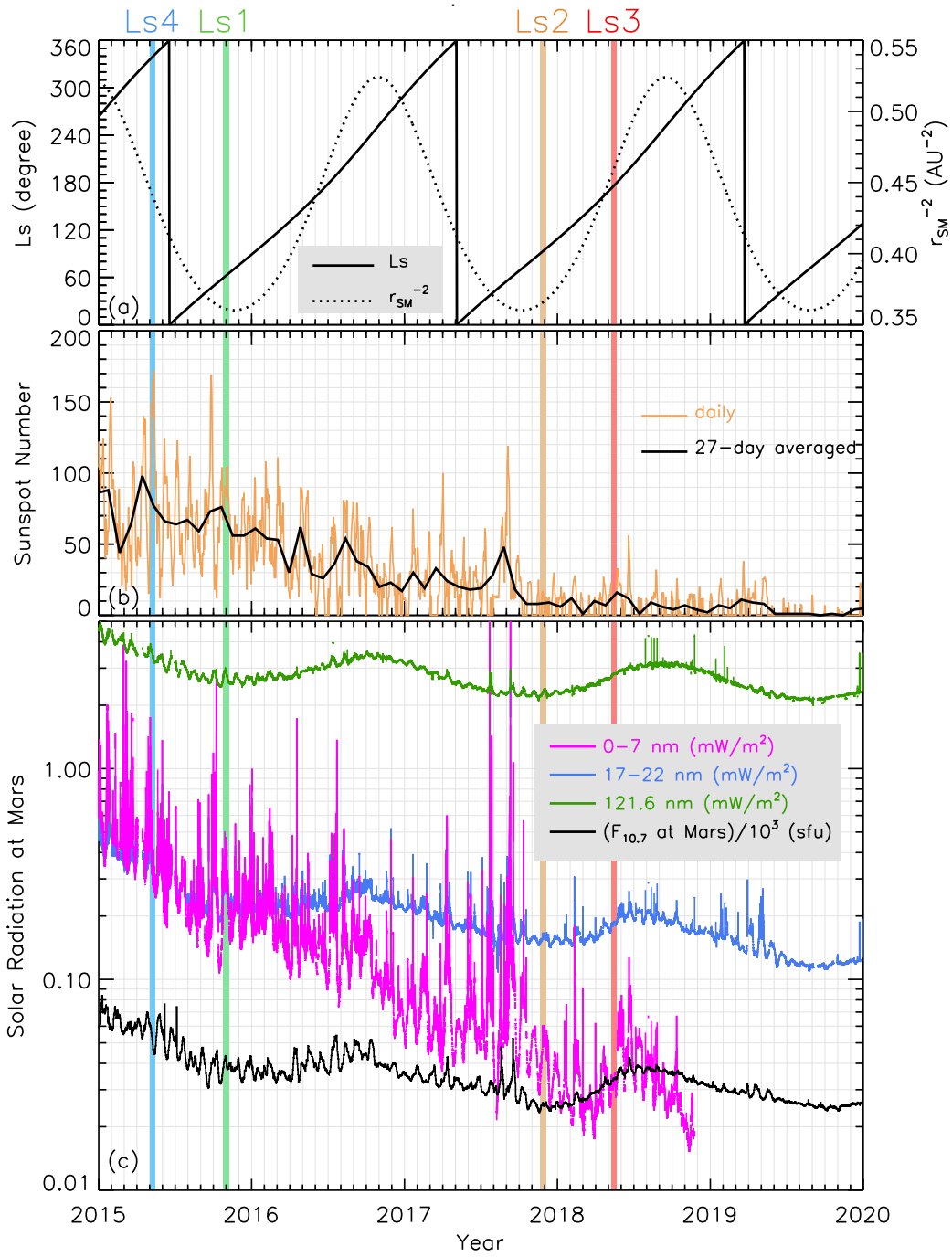

Figure S2. (a) Mars solar longitude (solid curve, left vertical axis) and the inverse square of the Sun-Mars distance (dotted curve, right vertical axis), as a function time. (b) Daily sunspot number (in yellow) and 27-day average sunspot number (in black). (c) Solar radiation at Mars above the atmosphere, including those directly measured by MAVEN EUVM channel A (17-22 nm, in blue), channel B (0-7 nm, in purple), channel C (121.6 nm, in green), and an indirect measure through $F_{10.7}$ that has been extrapolated from Earth to Mars (in black). The EUVM data are averaged at a 1-min cadence. In the extrapolation of $F_{10.7}$, we consider not only solar radiation decrease with the heliocentric distance but also the angular separation between Earth and Mars. Note that the $F_{10.7}$ index has been reduced by a factor of 10^3 to fit in the frame. In all the panels, the time intervals of the four cases that we study in this work (Ls1-Ls4) are highlighted by vertical shading bars. The corresponding mean values of the parameters are summarized in Table 1 of the main text.

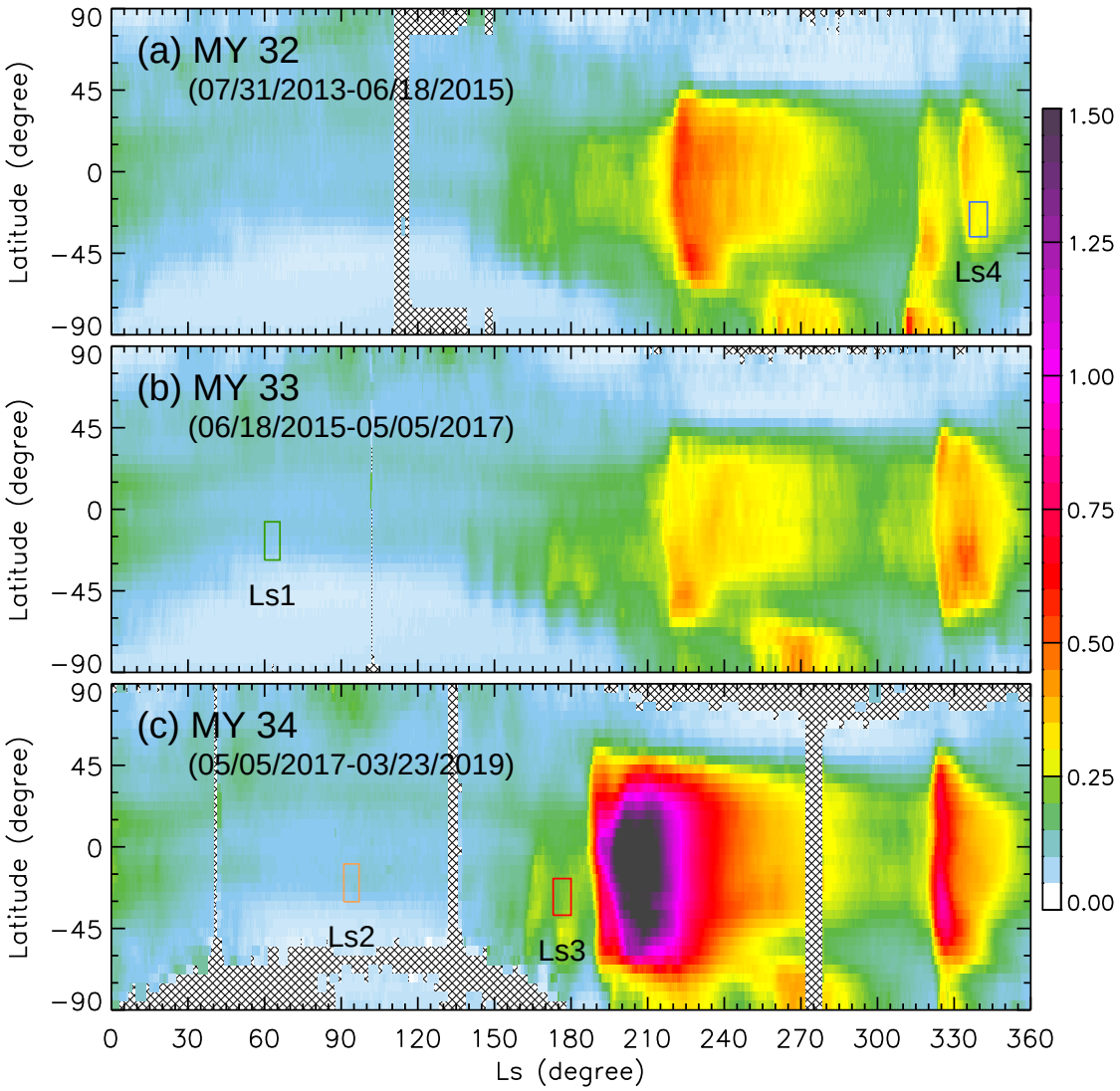

Figure S3. Mars zonally-averaged column dust optical depth at ∼9.3 μm as a function of solar longitude and latitude in three Martian years: (a) MY 32, (b) MY 33, and (c) MY 34. The dust opacity has been scaled to the atmospheric pressure level of 610 Pa (cf., Montabone et al., 2020). The cross-hatched areas indicate missing data. The MAVEN data coverage in the Ls-latitude space during the four cases of Ls1-Ls4 (which are scattered in the three Martian years) are marked by rectangles. The average dust opacities in the cases are given in Table 1 of the main text.

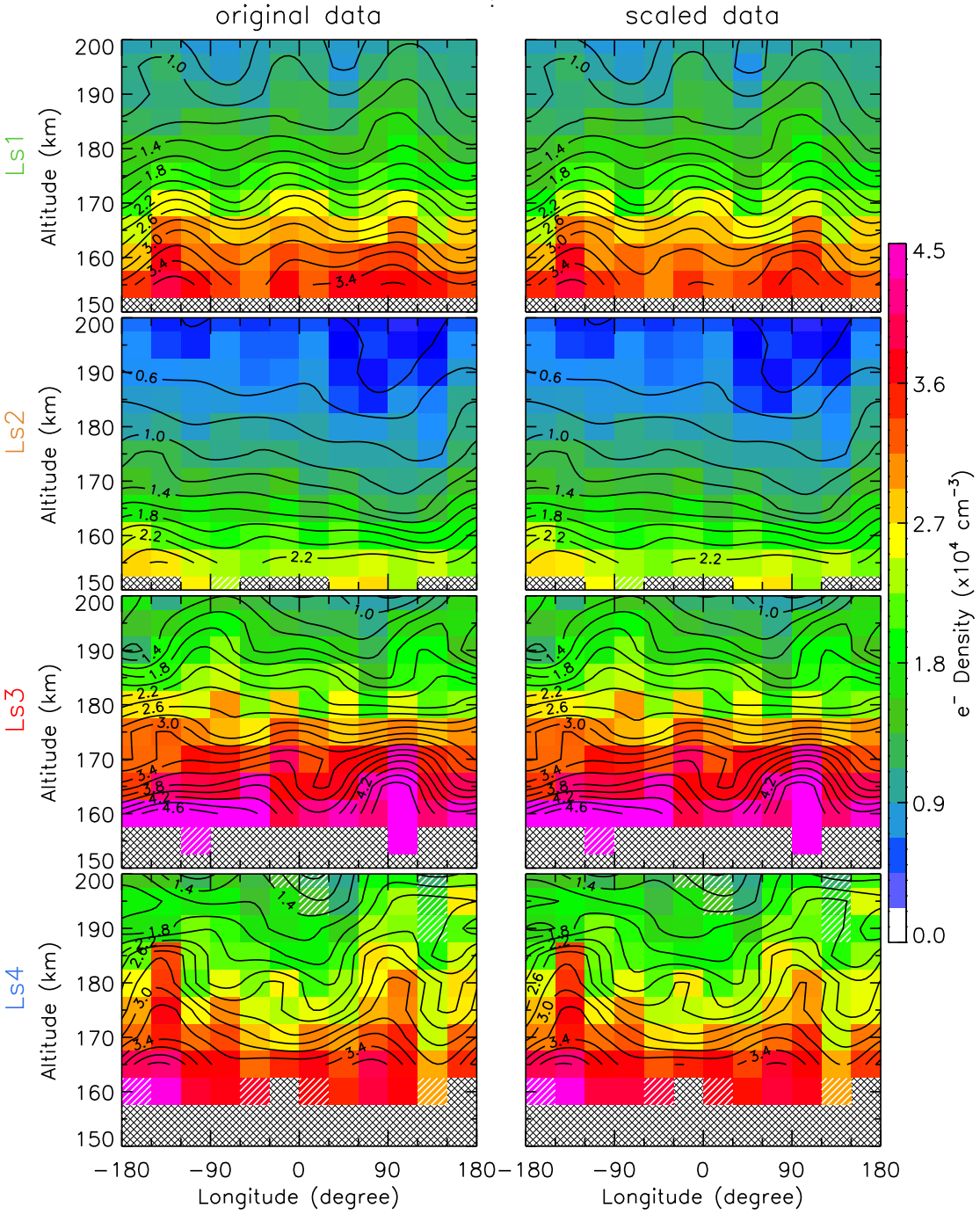

Figure S4. Comparison of the height-longitude structure of the electron density among the four cases: (from top to bottom) Ls1, Ls2, Ls3, Ls4. The two columns show the analysis using the original MAVEN LPW data and using the data that have been scaled to remove potential observational bias due to SZA and EUV differences. In the scaling with SZA, the density is multiplied by a factor to scale to the median SZA level within each case. The scaling factor, which is SZA- and altitude-dependent, is calculated from a time-dependent global MHD simulation of Ma et al. (2014); Fang et al. (2015, 2017). The factor is written as $n_{e\mathrm{MHD}}(\chi_{\mathrm{M}}, z)/n_{e\mathrm{MHD}}(\chi, z)$, where χ is SZA and χ_{M} stands for the median SZA value. In the scaling with EUV, the electron density is normalized to the median EUV level by multiplying by a scaling factor of sqrt($\mathrm{EUV_M}$/EUV). The solar radiation energy flux measured by the MAVEN EUVM channel A (17-22 nm) is used as the proxy of EUV. The cross-hatched areas indicate missing data.

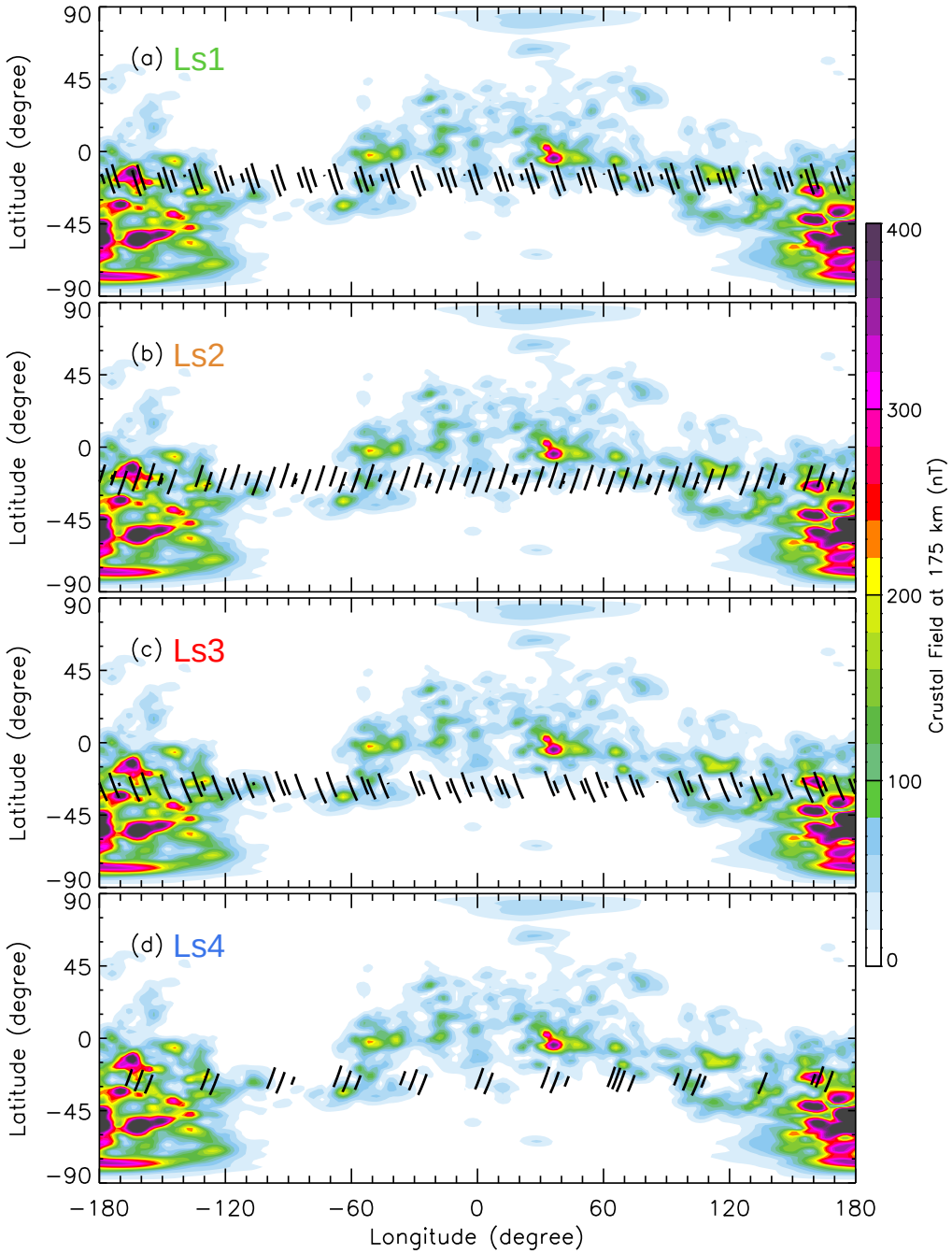

Figure S5. The projection of the selected MAVEN LPW orbital data on the longitude-latitude plane in (a) Ls1, (b) Ls2, (c) Ls3, and (d) Ls4. The background color contour shows the magnitude of the Martian crustal magnetic field at 175 km altitude, which is calculated using the model of Morschhauser et al. (2014).

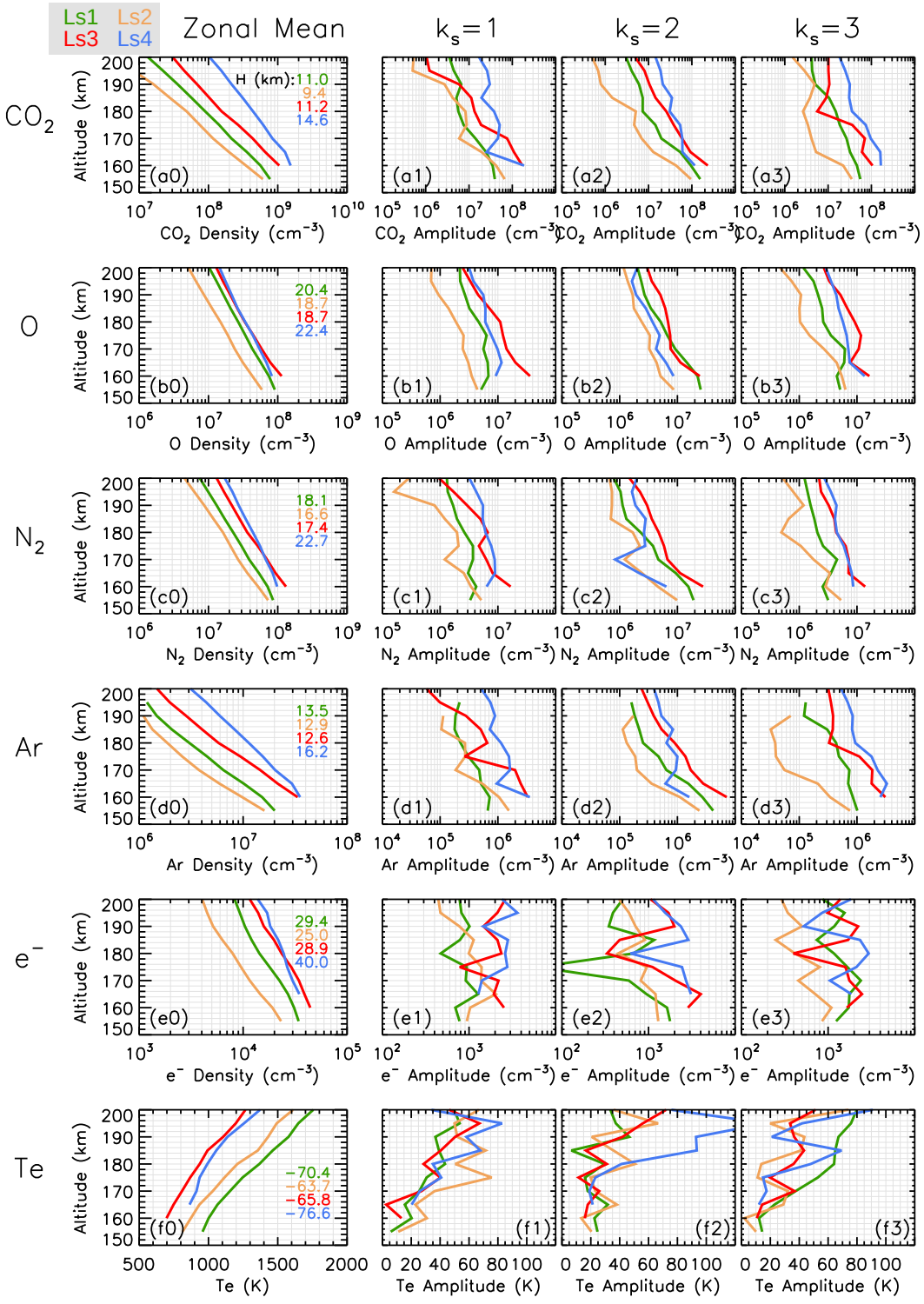

Figure S6. Similar to Figure 8 of the main text but showing absolute wave amplitudes.